ACS APPLIED MATERIALS & INTERFACES

Research Article

www.acsami.org

Electrodeposition of Antimony Selenide Thin Films and Application in Semiconductor Sensitized Solar Cells

T. Tuyen Ngo, Sudam Chavhan, Ivet Kosta, Oscar Miguel, Hans-Jurgen Grande, and Ramón Tena-Zaera*

IK4-CIDETEC, Parque Tecnológico de San Sebastián, Paseo Miramón 196, Donostia-San Sebastián, Gipuzkoa 20009, Spain

Supporting Information

ABSTRACT: Sb_2Se_3 thin films are proposed as an alternative light harvester for semiconductor sensitized solar cells. An innovative electrodeposition route, based on aqueous alkaline electrolytes, is presented to obtain amorphous Sb_2Se_3. The amorphous to crystalline phase transition takes place during a soft thermal annealing in Ar atmosphere. The potential of the Sb_2Se_3 electrodeposited thin films in semiconductor sensitized solar cells is evaluated by preparing $TiO_2/Sb_2Se_3/CuSCN$ planar heterojunction solar cells. The resulting devices generate electricity from the visible and NIR photons, exhibiting the external quantum efficiency onset close to 1050 nm. Although planar architecture is not optimized in terms of charge carrier collection, photocurrent as high as 18 mA/cm^2, under simulated (AM1.5G) solar light, is achieved. Furthermore, the effect of the Sb_2Se_3 thickness and microstructural properties on the photocurrent is analyzed, suggesting the hole transport is the main limiting mechanism. The present findings provide significant insights to design efficient semiconductor sensitized solar cells based on advanced architectures (e.g., nanostructured and tandem), opening wide possibilities for progresses in this emerging photovoltaics technology.

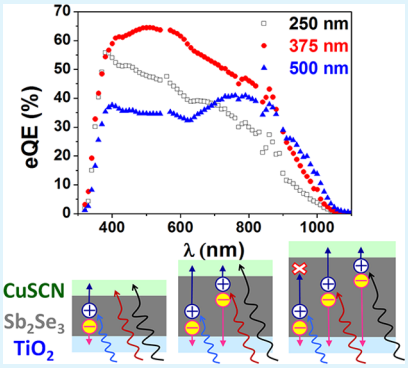

KEYWORDS: *Sb_2Se_3, solar cell, semiconductor sensitized, electrodeposition*

1. INTRODUCTION

VA-VIA group compound semiconductors have been extensively investigated in the field of thermoelectric applications.[1−3] However, some compounds of this family like Sb_2S_3, Bi_2S_3, and Sb_2Se_3 exhibit bandgap values well suited for photovoltaic devices being an attractive alternative to other chalcogenide compounds, e.g., CdTe, CdSe, PbS, or PbSe QDs, which contain toxic metals such as Cd and Pb considered as restricted substances by some regulations.[4] Indeed, after pioneering studies by Hodes's[5] and Larramona's[6] groups on Sb_2S_3-based semiconductor sensitized solar cells, there is a growing photovoltaic interest in this material. As a clear example of Sb_2S_3 potential, power conversion efficiencies higher than 6% in TiO_2/Sb_2S_3/polymer solar cells have been recently reported by Il Seok's group.[7] However, compared to Sb_2S_3, the Sb_2Se_3 exhibits a bandgap close to the ideal Shockley−Queisser value,[8] and recent theoretical studies predicted better performance in semiconductor sensitized solar cells.[9] Nevertheless, although a recent fundamental study shed some light on the photogeneration and transfer of the charge carriers in metal oxide/Sb_2Se_3/spiro-OMeTAD heterostructures,[10] reports on Sb_2Se_3-based semiconductor sensitized solar cells can be rarely found.[11]

Among the different synthetic approaches reported obtaining Sb_2Se_3,[10−18] electrodeposition appears to be a highly attractive technique to obtain not only thin films with controlled thickness but also uniform and conformal coatings on nanostructured substrates. As recently demonstrated for lead halide-based perovskites,[19−22] the versatility in the deposition method may provide significant added value for evaluating alternative materials in solar cells based on the different architectures and/or concepts. However, previous reports on the Sb_2Se_3 electrodeposition are based on the use of acidic solutions, which may limit the choice of the substrate. Furthermore, they propose selenium(IV) compounds, such as SeO_2,[21] and H_2SeO_3[14,24] as selenium precursor with the deposition of metal Se, via the four-electron reduction, and the consequent intermediate steps in the Sb_2Se_3 formation and/or interferences in the obtained films.

In this paper, an innovative electrodeposition route based on aqueous alkaline baths containing selenosulfate anions is presented to obtain Sb_2Se_3 thin films. Their potential as solar light harvester in semiconductor sensitized solar cells is evaluated by preparing and characterizing TiO_2/Sb_2Se_3/CuSCN planar heterojunction devices. The influence of the Sb_2Se_3 thickness and microstructural properties on the photocurrent is analyzed, pointing out the hole transport along the Sb_2Se_3 as the main limiting mechanism.

2. EXPERIMENTAL SECTION

2.1. Sb_2Se_3 Electrodeposition. The electrolyte was an aqueous 0.1 M ammonium buffer solution (pH ∼ 9.0) containing sodium selenosulfate and antimony in a complex form. Briefly, the selenosulfate solution was prepared according to the previously

Received: November 27, 2013
Accepted: January 17, 2014
Published: January 17, 2014

   dx.doi.org/10.1021/am405416a | ACS Appl. Mater. Interfaces 2014, 6, 2836−2841

reported procedure.[25] Secondly, a 2.5 mM antimony acetate (99.9% trace metals basis), 0.1 M potassium sodium tartrate tetrahydrate (regent plus ≥99%), and 0.1 M ammonium buffer was prepared. The full electrolyte was then prepared by mixing both solutions in a volume ratio of 7:3. The solution was bubbled with Ar prior to deposition for 15 minutes and during the electrochemical deposition process, which was performed in a three-electrode electrochemical cell with the substrate as the working electrode (cathode), a Pt spiral wire as the counter electrode, and a saturated calomel electrode (SCE) as the reference electrode. In the text, all the potentials are quoted versus SCE. Two types of substrates were used: commercial fluorine doped tin oxide glasses (FTO) (TEC15, Hartford Glass) and TiO_2 coated FTO. The thin compact TiO_2 layer was deposited on to FTO substrate by spray pyrolysis as reported in ref 26. For each working electrode, a well determined geometric surface was masked off prior to the cyclic voltammetry (CV) and electrodeposition experiments. Both were performed at room temperature by using a VMP3 BioLogic-Science Multichannel Workstation.

For CV, three scans for each cathode were carried out from solution rest potential (near zero), with a cathodic sweep to −1.5 V and then an anodic sweep to +0.5 V. When different scan limits were used, they are specifically mentioned in the text. The scan rate was 20 mV/s. Meanwhile, the charge density passed during the electrodeposition was varied in the range of 0.25−1 C/cm^2.

2.2. Thermal Annealing Treatments. Post-deposition thermal annealing processes were applied to some samples in an open horizontal tubular furnace, in the temperature range of 240−280°C for 20 minutes. Although the experiments were carried out under Ar flow, traces of residual air cannot fully be ruled out due to the particular geometry of the furnace (i.e., one side closed).

2.3. Thin Film Characterization. The morphology and structural properties of the films were analyzed using a ULTRA plus ZEISS field emission scanning electron microscope (FESEM) and a Bruker AXS-D8 Advance X-ray diffractometer (XRD) using Cu Kα radiation. The optical transmittance and reflectance of the films were measured at room temperature with a Jascow V-570 spectrophotometer fitted with an integrating sphere, from 300 to 1200 nm.

2.4. Solar Cell Preparation and Characterization. Solar cells based on the glass/FTO/$TiO_{2(compact)}$/Sb_2Se_3/CuSCN/Au planar heterojunction architecture were fabricated. The Sb_2Se_3 films were electrodeposited at room temperature at constant potential (V ∼ −0.94 V) by passing charge densities in the range of 0.25−1 C/cm^2. The CuSCN layer was deposited, from a saturated solution of CuSCN in propylsulfide,[27] on pre-heated ∼100 °C glass/SnO_2:F/TiO_2/Sb_2Se_3 samples. The amount of solution used in the CuSCN deposition process was in the range of 0.005−0.020 ml/cm^2. Finally, an array of gold dots, 0.35 cm in diameter, was deposited on the CuSCN layer by using an NANO38 thermal evaporator.

The current−voltage characteristic of the cells were measured using a xenon arc lamp simulator (Sun 2000, ABET Technologies) with an AM 1.5 G spectral filter, and the intensity was adjusted to provide 1 sun (100 mW/cm^2) using a calibrated silicon solar cell. The active area was defined to be 0.07 cm^2 by using a mask. The spectral response of the device photocurrent was measured using a computerized home-built setup (xenon arc lamp, chopper, monochromator, lock-in amplifier). The external quantum efficiency (eQE) was calculated using a standard Si photodiode.

3. RESULTS AND DISCUSSION

3.1. Electrodeposition of Antimony Selenide. At first, alkaline (pH ∼ 9) aqueous electrolytes containing sodium selenosulfate (Na_2SeSO_3), acting as a Se precursor, and stabilized antimony(III) complexes $Sb(CH_3COO)_3$, acting as Sb^{3+} precursor, plus $KNaC_4H_4O_6{\cdot}4H_2O$ were specifically formulated. The electrochemical behavior of a single precursor and full electrolytes was analyzed by cyclic voltammetry (CV), and the voltammograms are shown in the Figure 1. In selenosulfate electrolyte, the cathodic current detected for V <

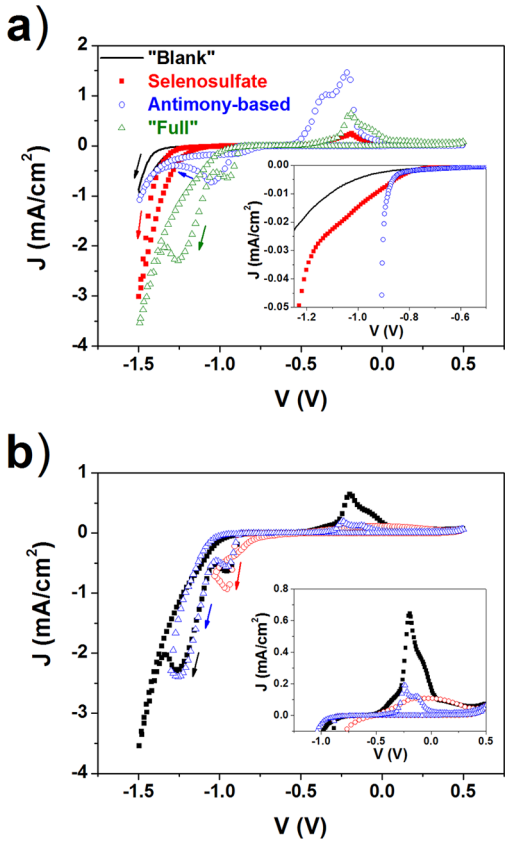

Figure 1. (a) Cyclic voltammograms of argon bubbled "blank" (−− 0.1 M NH_4Cl and 10^{-4} M NH_3 aqueous solution), "single-component" (i.e., selenosulfate (red ■, 0.4M Na_2SO_3, 0.2M Se aqueous solution) and antimony-based (blue ○, 0.1M NH_4Cl, 0.1 mM NH_3, 0.1M $KNaC_4H_4O_6{\cdot}4H_2O$, and 2.5 mM $Sb(CH_3COO)_3$ aqueous solution)) and "full" electrolytes (green △, i.e., selenosulfate and antimony-based solutions mixed 3:7 v/v). (b) Cyclic voltammograms of the full electrolyte recorded by using different scan potential ends. The inset shows a partially magnified view of the anodic sweep. The arrows indicate the sweep direction.

−0.75 V (Figure 1, inset) is attributed to the two-electron reduction of selenosulfate anions, i.e., the production of Se^{2-} by means of $SeSO_3^{2-}$ + 2 e^- = Se^{2-} + SO_2^{-}.[28] The anodic feature with the onset at ∼−0.4 V may be due to the electrochemical oxidation of the Se^{2-}, which suggests the good chemical stability of the latter in the electrolyte. This behavior differs significantly from that of selenium(IV) precursors, in which different waves are detected because of the formation of Se^0 and Se^{2-}.[14,23] The stability of Se^{2-} may be limited by the comproportionation reaction between the produced Se^{2-} and remaining Se^{4+}, resulting in the chemical formation of Se^0. However, in the present selenosulfate-based electrolyte, the Se^{2-} can be electrochemically produced and kept available for reacting with the stabilized Sb^{3+} in the full electrolyte. Nevertheless, as the cathodic current onset for selenosulfate and antimony-based single electrolytes occurred at similar potentials (Figure 1, inset), a clear potential window for the Sb_2Se_3 deposition by the chemical reaction between Sb^{3+} and Se^{2-} could not be anticipated. However, the voltammogram of the full electrolyte exhibited two well-defined cathodic waves, centered at ∼−0.94 and ∼−1.26 V, indicating the presence of two different electrochemical phenomena. In order to cast some light into their nature, CVs with different cathodic scan

ends were performed (Figure 1b). When the cathodic sweep was stopped at $V \sim -1.0$ V (i.e., after the first cathodic wave occurred), a relatively weak and broad anodic feature is detected (Figure 1b, inset). As this differs significantly from the antimony single electrolyte, the antimony deposition during the cathodic sweep did not seem to occur. This is not the case for the CV ending at $V < -1.3$ V (i.e., after the second cathodic wave occurred), in which the two-peak anodic feature with the most intense contribution, very similar to that from the single antimony electrolyte, is detected. Thus, the co-deposition of antimony and antimony–selenium compounds appears to be the most probable scenario at $V < -1.0$ V. Therefore, the potential of ~−0.94 V (i.e., the maximum of the first cathodic wave) was chosen for the potentiostatic electrodeposition experiments in order to avoid the Sb^0 in the films. As a result, grayish and homogenous films are obtained in a reproducible way.

3.2. Antimony Selenide Thin Film Characterization. Figure 2 shows FESEM micrographs of samples electro-

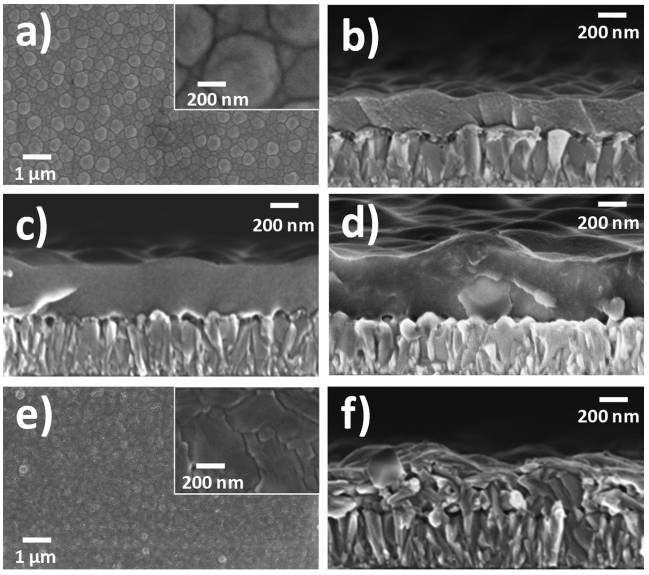

Figure 2. FESEM micrographs of as deposited (a–d) and annealed (e,f) samples. (a and e) Representative top views of as deposited and thermally annealed at 280 °C in Ar samples, respectively. (b–d) The cross-section view of as deposited films obtained by passing charge densities of 0.25, 0.5, and 1 C/cm^2, respectively. (f) The cross-section of the film obtained by passing 0.5 C/cm^2 and annealed at 280 °C in Ar atmosphere.

deposited, on to TiO_2 coated glass/FTO substrates, after passing 0.25, 0.5, and 1.0 C/cm^2 charge densities, and rough thin films with mean thicknesses of 250, 375, and 500 nm were obtained, respectively. Although granular-like features might be inferred from the top view micrographs (Figure 2a), the cross section micrographs (Figures 2b–d) pointed out that these morphological features are mainly due to differences in the local thickness and no grain boundaries are noticed. However, Figure 2e,f depicts new morphological features in annealed samples, suggesting the grain formation during the thermal treatment.

The structural properties of the samples were analyzed by X-ray diffraction (XRD) as shown in Figure 3. No additional features to the tetragonal SnO_2[29] and anatase TiO_2[30] phases from the substrates are detected for the as-deposited samples, but the antimonselite phase[31] is clearly found in XRD pattern

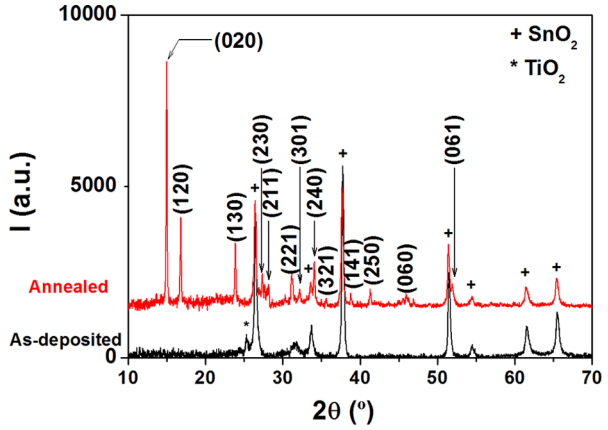

Figure 3. XRD pattern of as deposited and thermally annealed (280 °C in Ar atmosphere) samples. The thickness of Sb_2Se_3 films is ~250 nm in both samples.

of annealed samples. This finding reveals the amorphous to crystalline phase transition during the annealing process. Similar behavior was found for Sb_2Se_3 thin films obtained by some of the previously reported wet-chemistry-based deposition routes.[12,24] In addition to the morphological changes observed in the FESEM micrographs (Figure 2e vs. 2a), the microstructural transition resulting in a red shift, in the optical absorption of the films, is also noticed (Supporting Information, Figure S1). Figure 4 shows the transmittance

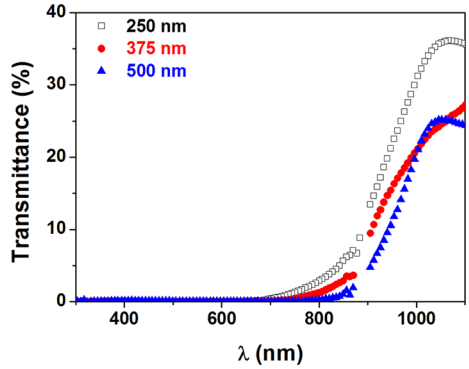

Figure 4. Transmittance spectra of glass/SnO_2:F/TiO_2/Sb_2Se_3 samples for different Sb_2Se_3 film thicknesses. All samples were annealed at 280 °C, in the presence of Ar, for 20 minutes.

spectra of samples of different thicknesses annealed at 280 °C. For wavelengths in the 700–1000 nm, a decrease of the transmittance as a function of the thickness is pointed out. As an example, at $\lambda \sim 950$ nm, the transmittance is 22%, 16%, and 11% for thicknesses of 250, 375, and 500 nm, respectively. Thus, the increase of the film thickness enhances significantly the absorption of the near infrared photons, as detected in the absorptance (i.e., $A = 100 - T - R$, where T and R are transmittance and reflectance, respectively) spectra (Supporting Information, Figure S2), suggesting that their absorption depth in the film may be larger than 375 nm.

3.3. Solar Cells. In order to evaluate the potential of the Sb_2Se_3 thin films in photovoltaic applications, solar cells based on the glass/FTO/TiO_2/Sb_2Se_3/CuSCN/Au planar heterojunction architecture were fabricated. Figure 5 shows the current density–voltage curves measured under AM1.5 simulated solar illumination for devices having different

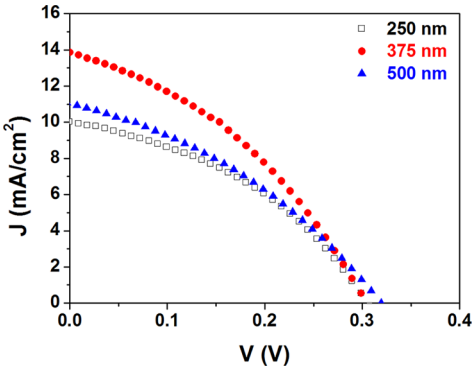

Figure 5. Photocurrent density−voltage curves, under simulated solar light (AM1.5G, 100 mW/cm^2), of solar cells based on different thicknesses of Sb_2Se_3 films.

thicknesses of Sb_2Se_3 photoactive layer. Table 1 summarizes the main photovoltaic parameters, i.e., short circuit photocurrent

Table 1

Sb_2Se_3 thickness [nm]	ann. temp. [°C]	J_{sc} [mA/cm^2]	V_{oc} [mV]	FF [%]	PCE [%]
250	280	10.0	305	39.7	1.2
375	280	13.8	304	37.6	1.6
500	280	11.0	319	35.9	1.3
375	240	10.0	326	38.5	1.3
375		0.82	266	32.4	0.1

(J_{sc}), open circuit voltage (V_{oc}), fill factor (FF), and power conversion efficiency (PCE) of representative devices from different series performed as a function of the Sb_2Se_3 thickness and annealing temperature. In general, the highest power conversion efficiency was obtained for devices based on the intermediate thickness (ca. 375 nm) of Sb_2Se_3 solar light harvester film. Moreover, as can be seen in Table 1, the annealing temperature is a crucial parameter which strongly influences the photovoltaic parameters, specifically photocurrent, of the device. As the most significant differences are detected in J_{sc}, the external quantum efficiency spectra were measured in order to gain further insight into the origin. Figure 6a shows the eQE spectra of the devices for which the $j-V$ curves are shown in Figure 5. In good agreement with the transmittance and absorptance spectra of the Sb_2Se_3 thin films (Figures 4 and S2, Supporting Information), a shift to longer wavelengths is observed in the eQE onset as the Sb_2Se_3 thickness increased. Interestingly, strong differences, i.e., ~35% vs. 65% for 500 and 375 nm, respectively, are found in the eQE spectra, in the 400−600 nm wavelengths range. Since the Sb_2Se_3 thin films exhibited very high light harvesting properties (i.e., negligible transmittance, Figure 3) in this wavelength range, differences in eQE spectra seem to be related to the charge carrier collection efficiency. This is also supported by the similar spectral features identified in the relative internal quantum efficiency (i.e., eQE versus absorptance before the Au contact deposition, Supporting Information Figure S3). Furthermore, as shown in Figure 6b, it is noticed that the eQE for wavelengths, in the 350−600 nm, is strongly dependent on the annealing temperature.

To shed some light on the relationship between the transmittance and eQE spectra, a model is proposed as shown in Figure 7. Blue and green (i.e., λ: 375−600 nm)

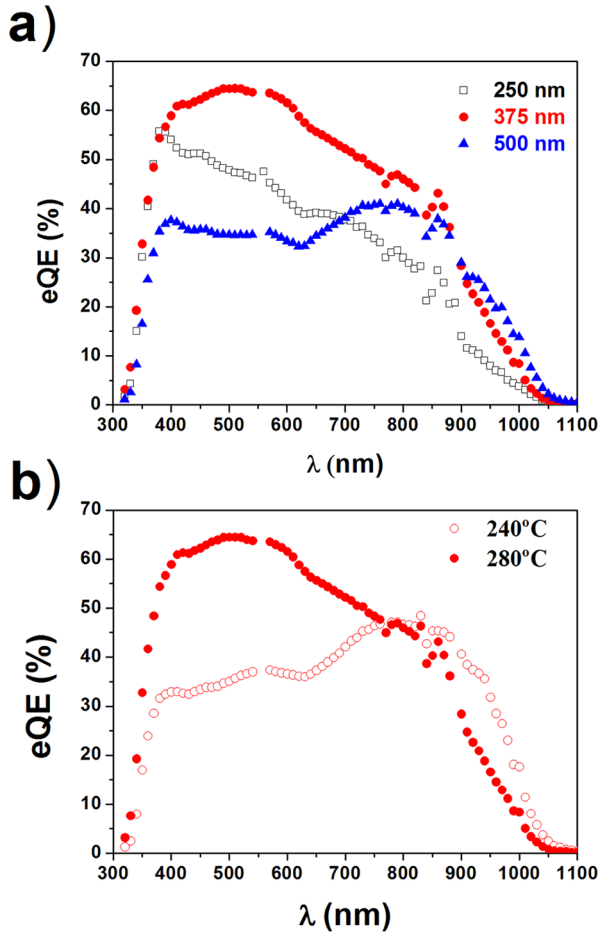

Figure 6. eQE of solar cells based on Sb_2Se_3 films (a) of different thicknesses (annealed at 280 °C, under Ar flow, for 20 minutes) and (b) annealed at different temperatures (375 nm thick).

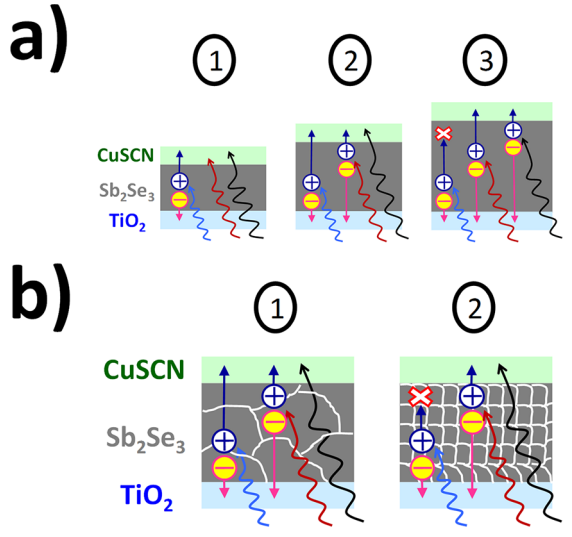

Figure 7. Schematic view of the photon absorption and charge carrier transport in solar cells based on Sb_2Se_3 films of different thicknesses (a) and crystallite size (b).

photons are absorbed relatively close to the TiO_2/Sb_2Se_3 interface. Therefore, once the exciton is dissociated, the holes need to be transported along the Sb_2Se_3 thin film before reaching CuSCN. A significant decrease of the quantum

dx.doi.org/10.1021/am405416a | ACS Appl. Mater. Interfaces 2014, 6, 2836−2841

efficiency for wavelengths lower than 600 nm detected in solar cells made up of 500 nm thick Sb_2Se_3 films seems to be due to the hole blocking in the light harvester film (Figure 7a-3) (i.e., hole diffusion length shorter than film thickness). Furthermore, the hole diffusion length seems to be significantly dependent on the microstructural properties of Sb_2Se_3 such as the crystallite size, and this appears to be the main reason for strong differences observed in eQE of devices in which Sb_2Se_3 films annealed at 240 and 280 °C as shown in Figure 6b. It is worth noting that a ~25% increase (i.e., from 42 to 54 nm[32]) in the crystallite size, which is estimated from the XRD patterns, is found for the Sb_2Se_3 thin films annealed at 280 °C versus those treated at 240 °C. Figure 7b displays a schematic view of the effect of the crystallite size, for a constant Sb_2Se_3 film thickness, on the transport of the photogenerated charge carriers by the absorption of the different wavelength photons.

In contrast to the blue photons, the absorption of red and NIR photons takes place relatively far from the TiO_2/Sb_2Se_3 interface, resulting in an increase of the electron pathway before the injection to the TiO_2. As the difference between the eQE spectra of devices annealed at different temperature (240 vs. 280 °C) decrease significantly for wavelengths >650 nm, the electron transport seems to be less sensitive to the microstructural properties of Sb_2Se_3 than the hole transport process. This is the expected behavior for Sb_2Se_3 because of its n-type semiconducting properties, i.e., electrons are the major charge carriers. Although the optoelectronic properties of amorphous and crystalline may be significantly different, it is worth noting that the eQE spectrum of the solar cells based on as deposited (i.e., amorphous) Sb_2Se_3 films (Supporting Information, Figure S4) shows only significant efficiency for wavelengths ≥600 nm. Thus, only charge carriers generated from photons absorbed relatively close to the Sb_2Se_3/CuSCN interface (i.e., minimized hole transport distance along the Sb_2Se_3 film) are partially collected in amorphous Sb_2Se_3-based devices. However, charge carrier collection is not found from blue and green photons, which points out that the hole transport process along the amorphous Sb_2Se_3 layer is not possible.

Taking advantage of the above Sb_2Se_3 optimization study and preliminary optimization of the TiO_2 and CuSCN thicknesses, glass/FTO/TiO_2/Sb_2Se_3/CuSCN/Au planar heterojunction (Supporting Information, Figure S5) solar cells with enhanced photocurrent were obtained. As an example, Figure 8 shows the $j-V$ curve and eQE spectrum of the best device. It is worth highlighting that J_{sc} equal to 18 mA/cm^2 is achieved. Although the present study is limited to the planar heterojunction architecture, which is not optimized for nanocrystalline films in terms of the solar light harvesting and photogenerated charge carrier collection, the reached photocurrent is much higher than those previously reported for fully inorganic semiconductor sensitized solar cells (e.g., TiO_2/Sb_2S_3/CuSCN,[5,33] ZnO/In_2S_3/CuSCN,[34] and ZnO/In_2S_3/$CuInS_2$[35]). Indeed, the J_{sc} is similar to values reported for the state of the art of the inorganic semiconductor sensitized solar cells based on liquid[36] and organic[7] hole conductors. Furthermore, the photocurrent also sounds to be comparable to those recently reported for the promising inorganic–organic perovskite solar cells.[19−22,37] However, the modest V_{oc} and FF values obtained from glass/FTO/TiO_2/Sb_2Se_3/CuSCN/Au heterojunction devices are limiting their PCE (η = 2.1%). Although accurate studies by using specific characterization techniques such as the recently proposed chemically resolved electrical measurements[38] is needed in order to determine the maximum V_{oc} in the TiO_2/Sb_2Se_3/CuSCN heterojunctions, significant improvements may be expected by the decrease of the recombination losses by further device optimization, i.e., especially hole conductor thin film properties, indicated in Supporting Information Figure S5, as an example of the wide room for improvement in the CuSCN films. The very low (<40%) FF, which is significantly lower compared to solar cells fabricated by using CuSCN (ca. 50%)[5,27,34,39] and other hole conductors such as P3HT[40] and spiro-MeOTAD,[41] also supports the presence of significant extra recombination pathways in present devices.

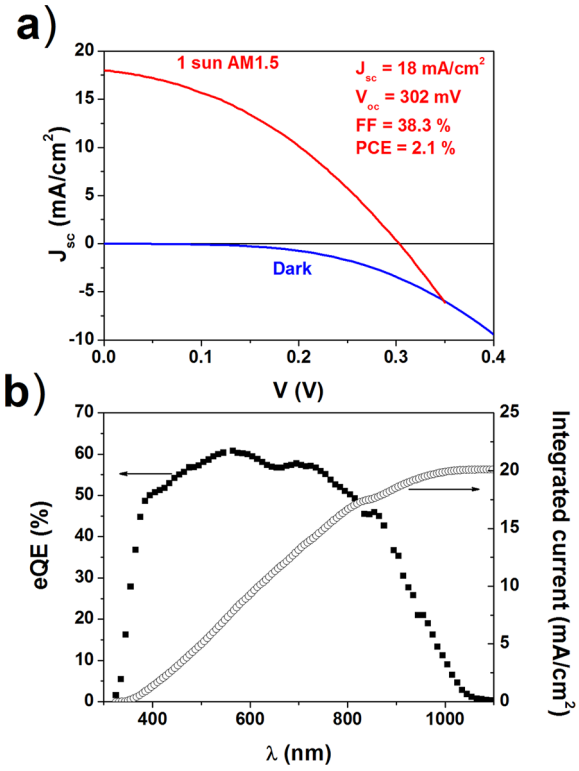

Figure 8. (a) Current density–voltage characteristics in dark and under simulated solar light (AM1.5G, 100 mW/cm^2) and (b) eQE spectrum for the best devices. The integrated current, from the eQE spectrum, is also displayed.

4. CONCLUSION

The significant potential of electrodeposited Sb_2Se_3 thin films in semiconductor sensitized solar cells has been demonstrated by using glass/FTO/TiO_2/Sb_2Se_3/CuSCN/Au heterojunction devices as a testing system. Considerably high photocurrent (J_{sc} ~ 18 mA/cm^2) has been achieved by the conversion of visible and NIR photons into electricity. As the working spectral range appears to be complementary to the most of the previously reported semiconductor sensitized solar cells, the use of Sb_2Se_3 as a solar light harvester may open wide possibilities for advanced device architectures (e.g., tandem). Tandem and/or nanostructured architectures may be specially designed in order to minimize the hole transport in the Sb_2Se_3, which has been suggested here as the main limiting mechanism. By this way, further improvements in the device performance and relaxation of the Sb_2Se_3 microstructural quality requirements, with the concomitant decrease of the annealing temperature and/or suppression of thermal treatments, may be expected.

■ ASSOCIATED CONTENT

Supporting Information

Some transmittance, absorptance, and relative internal and external quantum efficiency spectra and FESEM of the device cross section. This information is available free of charge via the Internet at http://pubs.acs.org/.

■ AUTHOR INFORMATION

Corresponding Author

*E-mail: rtena@cidetec.es.

Author Contributions

The manuscript was written through contributions of all authors. All authors have given approval to the final version of the manuscript.

Notes

The authors declare no competing financial interest.

■ ACKNOWLEDGMENTS

This work was partially funded by Ministerio de Ciencia e Innovación of Spain (MICINN) and Basque Regional Government through HOPE CSD2007-00007 (Consolider-Ingenio 2010) project and Etortek Programme, respectively. R.T-Z. acknowledges the support from the "Ramón and Cajal" Programme of the MICINN.

■ REFERENCES

(1) Mahan, G. D. *Solid State Phys.* **1998**, *541*, 81−157.
(2) Venkatasubramanian, R.; Siivola, E.; Colpitts, T.; Quinn, B. *Nature* **2001**, *413*, 597−602.
(3) Mastrovito, C.; Lekse, J.W.; Aitken, J.A. *J. Solid State Chem.* **2007**, *180*, 3262−3270.
(4) The Restriction of Hazardous Substances Directive 2002/95/EC (http://ec.europa.eu/enterprise/policies/european-standards/harmonised-standards/restriction-of-hazardous-substances). (Accessed July 1, 2011).
(5) Itzhaik, Y.; Niitsoo, O.; Page, M.; Hodes, G. *J. Phys. Chem. C* **2009**, *113*, 4254−4256.
(6) Chone, C.; Larramona, G. (IMRA Europe), French Patent 2899385, 05, October 2007.
(7) Im, S. H.; Lim, C.-S.; Chang, J. A.; Lee, Y. H.; Maiti, N.; Kim, H.-J.; Nazeeruddin, Md. K.; Gratzel, M.; Il Seok, S. *Nano Lett.* **2011**, *11*, 4789−4793.
(8) Shockley, W.; Queisser, H. J. *J. Appl. Phys.* **1961**, *32*, 510−519.
(9) Patrick, C. E.; Giustino, F. *Adv. Funct. Mater.* **2011**, *21*, 4663−4667.
(10) Guijarro, N.; Lutz, T.; Lana-Villarreal, T.; O'Mahony, F.; Gomez, R.; Haque, S. A. *J. Phys. Chem. Lett.* **2012**, *3*, 1351−1356.
(11) Choi, Y. C.; Mandal, T. N.; Yang W. S. ; Lee, Y. H.; Im, S. M.; Noh, J. H. ; Il Seok, S. *Angew. Chem., Int. Ed.* **2014**, DOI: 10.1002/anie.201308331, published online during the revision of this paper.
(12) Messina, S.; Nair, M. T. S.; Nair, P. K. *J. Electrochem. Soc.* **2009**, *156*, H327−H332.
(13) Torane, A. P.; Rajpure, K. Y.; Bhosale, C. H. *Mater. Chem. Phys.* **1999**, *61*, 219−222.
(14) Lai, Y.; Han, C.; Lv, X.; Yang, J.; Liu, F.; Li, Y.; Liu, J. *J. Electroanal. Chem.* **2012**, *671*, 73−79.
(15) Sankapal, B. R.; Lokhande, C. D. *Sol. Energy Mater. Sol. Cells* **2001**, *69*, 43−52.
(16) Lokhande, C. D.; Sankapal, B. R.; Sartale, S. D.; Pathan, H. M.; Giersig, M.; Ganesan, V. *Appl. Surf. Sci.* **2001**, *182*, 413−417.
(17) Rajpure, K. Y.; Lokhande, C. D.; Bhosale, C. H. *Mater. Res. Bull.* **1999**, *34*, 1079−1087.
(18) Xue, M.-Z.; Fu, Z.-W. *J. Alloys Compd.* **2008**, *458*, 351−356.
(19) Kim, H.-S.; Lee, C.-R.; Im, J.-H.; Lee1, K.-B.; Moehl, T.; Marchioro, A.; Moon, S.-J.; Humphry-Baker, R.; Yum, J.-H.; Moser, J. E.; Gratzel, M.; Park, N.-G. *Sci. Rep.* **2012**, *2*, 591−598.
(20) Ball, J. M.; Lee, M. M.; Hey, A.; Snaith, H. J. *Energy Environ. Sci.* **2013**, *6*, 1739−1743.
(21) Burschka, J.; Pellet, N.; Moon, S.-J.; Humphry-Baker, R.; Gao, P.; Nazeeruddin, Md. K.; Gratzel, M. *Nature* **2013**, *499*, 316−319.
(22) Eperon, G. E.; Burlakov, V. M.; Docampo, P.; Goriely, A.; Snaith, H. J. *Adv. Funct. Mater.* **2013**, DOI: 10.1002/adfm.201302090.
(23) Li, J.; Wang, B.; Liu, F.; Yang, J.; Li, J.; Liu, J.; Jia, M.; Lai, Y.; Liu, Y. *Electrochim. Acta* **2011**, *56*, 8597−8602.
(24) Lai, Y.; Chen, Z.; Han, C.; Jiang, L.; Liu, F.; Li, J.; Liu, Y. *Appl. Surf. Sci.* **2012**, *261*, 510−514.
(25) Hodes, G.; Grunbaum, E.; Feldman, Y.; Bastide, S.; Lévy-Clément, C. *J. Electrochem. Soc.* **2005**, *152*, G917−G923.
(26) González-Pedro, V.; Sima, C.; Marzari, G.; Boix, P. P.; Giménez, S.; Shen, Q.; Dittrich, T.; Mora-Sero, I. *Phys. Chem. Chem. Phys.* **2013**, *15*, 13835−13843.
(27) Mora-Sero, I.; Gimenez, S.; Fabregat-Santiago, F.; Azaceta, E.; Tena-Zaera, R.; Bisquert, J. *Phys. Chem. Chem. Phys.* **2011**, *13*, 7131−7138.
(28) Kutzmutz, S.; Lang, G.; Heusler, K. *Electrochim. Acta* **2011**, *47*, 955−965.
(29) Powder Diffraction File 00-041-1445, PDF-2 Database Sets; International Center for Diffraction Data: Newton Square, PA, 1993.
(30) Powder Diffraction File 01-089-4203, PDF-2 Database Sets; International Center for Diffraction Data: Newton Square, PA, 1993.
(31) Powder Diffraction File 00-015-0861, PDF-2 Database Sets; International Center for Diffraction Data: Newton Square, PA, 1993.
(32) It is noted that the estimated crystallite size values can be slightly underestimated because the instrumental contributions to the XRD peak broadening was not considered.
(33) Nezu, S.; Larramona, G.; Chone, C.; Jacob, A.; Delatouche, B.; Père, D.; Moisan, C. *J. Phys. Chem. C* **2010**, *114*, 6854−6859.
(34) Dittrich, T.; Kieven, D.; Rusu, M.; Belaidi, A.; Tornow, J.; Schwarzburg, K.; Lux-Steiner, M. *Appl. Phys. Lett.* **2008**, *93*, 053113.
(35) Krunks, M.; Karber, E.; Katerski, A.; Otto, K.; Oja Acik, I.; Dedova, T.; Mere, A. *Sol. Energy Mater. Sol. Cells* **2010**, *94*, 1191−1195.
(36) Wang, J.; Mora-Sero, I.; Pan, Z.; Zhao, K.; Zhang, H.; Feng, Y.; Yang, G.; Zhong, X.; Bisquert, J. *J. Am. Chem. Soc.* **2013**, *135*, 15913−15922.
(37) Liu, M.; Johnston, M. B.; Snaith, H. J. *Nature* **2013**, *501*, 395−398.
(38) Itzhaik, Y.; Hodes, G.; Cohen, H. *J. Phys. Chem. Lett.* **2011**, *2*, 2872−2876.
(39) Larramona, G.; Chone, C.; Jacob, A.; Sakakura, D.; Delatouche, B.; Pere, D.; Cieren, X.; Nagino, M.; Bayon, R. *Chem. Mater.* **2006**, *18*, 1688−1696.
(40) Chang, J. A.; Rhee, J. H.; Im, S. H.; Lee, Y. H.; Kim, H.-J.; Il Seok, S.; Nazeeruddin, Md. K.; Gratzel, M. *Nano Lett.* **2010**, *10*, 2609−2612.
(41) Moon, S.-J.; Itzhaik, Y.; Yum, J.-H.; Zakeeruddin, S. M.; Hodes, G.; Gratzel, M. *J. Phys. Chem. Lett.* **2010**, *1*, 1524−1527.